Kim *et al. Soft Sci* 2022;2:8
DOI: 10.20517/ss.2022.06

Soft Science

Research Article

Open Access

Check for updates

Biocompatible composite thin-film wearable piezoelectric pressure sensor for monitoring of physiological and muscle motions

Nam-In Kim[1,2,3,4,#], Jong Moon Lee[5,#], Mina Moradnia[2,3,4], Jie Chen[2,3,4], Sara Pouladi[2,3,4], Miad Yarali[1,2,3,4], Ja Yeon Kim[6], Min-Ki Kwon[7], T. Randall Lee[5,*], Jae-Hyun Ryou[1,2,3,4,8,*]

[1]Materials Science and Engineering Program, University of Houston, Houston, TX 77204-4006, USA.
[2]Department of Mechanical Engineering, University of Houston, Houston, TX 77204-4006, USA.
[3]Texas Center for Superconductivity at UH (TcSUH), University of Houston, Houston, TX 77204, USA.
[4]Advanced Manufacturing Institute (AMI), University of Houston, Houston, TX 77204, USA.
[5]Department of Chemistry, University of Houston, Houston, TX 77204-5003, USA.
[6]Korea Photonics Technology Institute (KOPTI), Gwangju 61007, South Korea.
[7]Department of Photonic Engineering, Chosun University, Gwangju 61452, South Korea.
[8]Department of Electrical & Computer Engineering, University of Houston, Houston, TX 77204-4006, USA.
[#]Authors contributed equally.

[*]**Correspondence to:** Prof. T. Randall Lee, Department of Chemistry, University of Houston, 4800 Calhoun Road, Houston, TX 77204-5003, USA. E-mail: trlee@uh.edu; Prof. Jae-Hyun Ryou, Department of Mechanical Engineering, University of Houston, 4800 Calhoun Road, Houston, TX 77204-4006, USA. E-mail: jryou@uh.edu

How to cite this article: Kim NI, Lee JM, Moradnia M, Chen J, Pouladi S, Yarali M, Kim JY, Kwon MK, Lee TR, Ryou JH. Biocompatible composite thin-film wearable piezoelectric pressure sensor for monitoring of physiological and muscle motions. *Soft Sci* 2022;2:8. https://dx.doi.org/10.20517/ss.2022.06

Received: 19 Apr 2022 **First Decision:** 20 May 2022 **Revised:** 9 Jun 2022 **Accepted:** 17 Jun 2022 **Published:** 26 Jun 2022

Academic Editor: Chuan Fei Guo **Copy Editor:** Fangling Lan **Production Editor:** Fangling Lan

Abstract

Whereas piezoelectric pressure sensors (PPSs) have been applied in the monitoring of human body movement and physiological parameters, they show inherent limitations in wearable applications, including toxicity, degradation, and brittleness. In this study, we develop safe, stable, and mechanically flexible composite thin films consisting of polyvinylidene fluoride (PVDF), $BaTiO_3$ nanoparticles (BTO-NPs), and textured aluminum nitride (AlN) thin film for the demonstration of wearable PPS with enhanced output performance and biocompatibility. The PPS made of BTO-NP-embedded-PVDF and AlN film on Cu foil is attached to different parts of human body to measure different output voltages depending on the physiological and physical stimulus. The simple bending (from breathing, chewing, and swallowing), joint motions (at wrist, elbow, and finger), and low- (from eyeball movement) and high-pressure applications (by squat, lunge, and walking) are measured. Our PVDF+BTO-NP/AlN-PPS (PBA-PPS) device has the potential for personal safety, healthcare, and activity monitoring applications with easy wearability.

Keywords: Wearable electronics, $BaTiO_3$-embedded PVDF, $BaTiO_3$/PVDF/AlN flexible piezoelectric pressure sensor, sputtered AlN thin films, human motion monitoring

INTRODUCTION

Wearable and skin-attachable piezoelectric pressure sensors (PPSs), which convert mechanical energy into electrical energy (especially voltage), offer several benefits in personal healthcare and safety systems, such as sensitive response to stress/strain, self-powered, low-cost, easily-expandable, portable, and secure properties. Therefore, PPSs have been developed for the detection of physical and physiological signals such as blood pressure[1-5], respiration[6,7], muscle motion[8,9], heart rate[4,10,11], joint motion[12-15], and so on. Various piezoelectric materials, including lead zirconate titanate ($Pb[Zr_xTi_{1-x}]O_3$, PZT)[3], zinc oxide (ZnO)[16,17], barium titanate ($BaTiO_3$, BTO)[8,18], polyvinylidene fluoride (PVDF)[6,19], and single-crystalline Group-III-nitrides (III-Ns)[10,20], have been employed for the development of PPSs. Among them, PZT has been most widely adopted due to its excellent piezoelectric properties. However, PZT-based PPSs raise serious safety concerns in wearable applications, while they can be used in other general applications for containing a substantial amount (~20%) of a toxic element, lead (Pb). Skin-contacting wearable sensors should be free from harmful elements because deleterious materials can be absorbed into the human body. ZnO poses no harm to health; however, it is not chemically stable[21]. Devices based on ZnO are prone to degradation, which makes such devices more suitable for transient electronics instead of wearable applications[21].

Other piezoelectric materials, PVDF, BTO, and III-N thin films, can be considered alternatives to PZT and ZnO. They are relatively stable and non-toxic, and can be mechanically flexible. However, each of them also possesses its own intrinsic limitation. Although PVDF polymers have excellent flexibility, they show low-efficiency piezoelectric conversion that is insufficient to generate substantial output voltage from a mechanical stimulus. BTO has high piezoelectric coefficients (similar to PZT), but its flexibility is limited, which makes the sensor difficult to attach to the skin. Single-crystalline III-N thin films have been reported for excellent performance in energy harvesting applications[22]. However, the fabrication of single-crystalline III-N films relies on rather a complicated process consisting of epitaxial growth followed by a layer-transfer technique[23]. Therefore, most III-N films for piezoelectric applications are deposited by sputtering[24,25], which leads to *c*-axis textured but not single-crystalline films. The crystalline defects of polycrystalline III-N materials cause leakage currents between the top and bottom electrodes that degrade the piezoelectric output[26,27].

In the present study, we integrate III-N film with BTO nanoparticles (BTO-NPs) encapsulated in PVDF films (i.e., PVDF+BTO-NP/AlN (PBA) composite films) to demonstrate working PPSs for various wearable applications to overcome the limitation of each material. The PBA films generate improved output voltages compared to PVDF films and minimize the leakage current of sputtered AlN films. Our PBA sensor is applied to monitor human physiological signals and movements, including skin contour changes (from breathing, chewing, swallowing, and eye movements), joint motion (at the wrist, elbow, and finger), and high-pressure movements (from squatting, lunging, and walking).

EXPERIMENTAL

Figure 1 illustrates the steps used to prepare the PBA sensors, including AlN sputtering deposition on Cu foil substrates [Figure 1A], synthesis of BTO-NP-embedded PVDF films on AlN/Cu [Figure 1B and C], and fabrication of the PPS devices [Figure 1D-F].

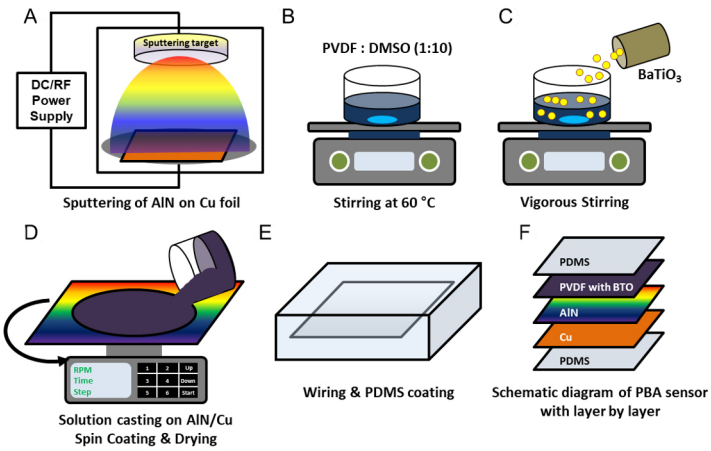

Figure 1. Illustration of the steps used to prepare the PBA sensor. (A) AlN sputtering deposition on Cu foil; (B) PVDF solution; (C) BTO-NP dispersion in PVDF; (D) PVDF+BTO-NP solution casting on AlN/Cu foil then spin coating and drying of PVDF+BTO-NP film; (E) wiring and PDMS sealing; and (F) Schematic diagram of PBA sensor. PBA: PVDF+BTO-NP/AlN; AlN: aluminum nitride; BTO-NP: $BaTiO_3$ nanoparticle; PVDF: polyvinylidene fluoride.

AlN film deposition

AlN thin films were deposited on 60-μm-thick Cu foil (American Elements, CA, USA) by DC reactive magnetron sputtering (AJA International) equipped with a DC power supply (Advanced Energy MDX 500). Before the sputtering, pre-sputtering was carried out to clean the aluminum (Al) target (1.5-inch diameter, 99.5%, AJA International) using argon-ion (Ar^+) bombardment. The pressure of the sputtering chamber was controlled at 10^{-9} Torr and 2 mTorr for base and working conditions, respectively. The working pressure was set by adjusting a gate valve of a cryopump. The AlN films were deposited at a DC cathode power of 110 W in plasma consisting of Ar and nitrogen (N_2) mixture, which were introduced into the chamber by separate mass flow controllers. The sample holder was automatically rotated at 20 revolutions per minute (rpm) during deposition to obtain a uniform AlN film with a thickness of ~200 nm. After the deposition, post-sputtering was performed to prevent the poisoning of the Al target.

Synthesis of PVDF-$BaTiO_3$ films on AlN

BTO-NPs were synthesized by modifying a previously reported method based on two metal precursors, $BaCl_2{\cdot}2H_2O$ and $TiCl_4$[28]. Polyvinylpyrrolidone (PVP) was used as a surfactant in the presence of sodium hydroxide (NaOH). An aqueous solution of $BaCl_2{\cdot}2H_2O$ was mixed with PVP at room temperature. Once the PVP was completely dissolved, the mixture was cooled in an ice bath, and then $TiCl_4$ was added while stirring. NaOH solution was gradually added to the mixture heated to 80 °C using a syringe pump, stirring constantly for 1 h. The solution was washed and centrifuged (6000 rpm for 10 min) twice with deionized water and then twice with ethanol. The precipitates (BTO-NPs) on the bottom of the container were collected and dried in the oven at 60 °C for 24 h.

BTO-embedded PVDF films were prepared by a simple spin-coating technique. PVDF pellets (15 wt.%) were completely dissolved in dimethylsulfoxide (DMSO) at 60 °C with vigorous stirring, followed by the addition of BTO-NPs (5, 10, and 30 wt.%). Once the BTO-NPs were uniformly dispersed in the PVDF solution, the mixture was spin-coated on an AlN/Cu film at 2500 rpm for 30 seconds and then dried in air. The thickness of PVDF+BTO-NP film was ~10 μm. Electric poling was conducted using a high-voltage power supply (PS325, Stanford Research Systems, CA, USA). For electric poling, wires of the PBA sensor were connected to a power supply, and then the output potential of the power supply was gradually increased from 0 to 2.5 kV then maintained for 1 h.

PPS device fabrication

A Cu foil substrate served as a bottom electrode. Silver wires were connected using silver paste (Ted Pella, CA, USA) and conductive Cu tape (3 M, single-sided) on both top and bottom electrodes. Then, liquid PDMS (Dow Corning Sylgard 184) was mixed with curing agent at a weight ratio of 10:1, and the mixed suspension was slowly dropped on the fabricated sensor to seal the device. Then, the packaged PBA sensor was placed in an electric oven at 90 °C for 3 h for curing. A biocompatible tape (3 M clear medical tape roll, double-sided) was used for the attachment of the PPS device to the volunteer's skin.

Structural characterizations of films

The phases of the PVDF film were characterized by Fourier-transform infrared spectroscopy (FTIR) using an attenuated total reflectance infrared spectroscope (ATR-IR, Nicolet iS10, Thermo Fisher Scientific, MA, USA) in the range of 500-1500 cm^{-1} at a resolution of 2 cm^{-1}. The crystal structure and quality of the deposited AlN thin film, PVDF, and BTO-NP-embedded PVDF were characterized using a high-resolution X-ray diffractometer (Bruker D8 Discover). The surface of the BTO-NP-containing PVDF film was observed by an optical microscope (Nikon Eclipse LV100ND) to monitor the differences in morphology originating from the various BTO contents.

Piezoelectric property characterizations

The prepared PVDF+BTO-NP/AlN-PPS (PBA-PPS) device was deflected by a custom-made piezoelectric test station composed of a digital micrometer drive (Mitutoyo) and a program-controlled motor (Anaheim Automation). The electrical signals from the sensor with different types of bending and force were measured by an electrometer (Keithley 6514) with LabVIEW-based software.

RESULTS AND DISCUSSION

Materials characterizations

Figure 2A shows the FTIR spectrum of the BTO-NP-embedded PVDF films. Different phases of PVDF can be identified by the specific wavenumbers of the peaks at 1431, 1275, 1234, 840, 812, 763, and 510 cm^{-1} corresponding to β + γ, β, γ, β + γ, γ, α, and β + γ phases, respectively. Four common peaks for all the phases of PVDF were also observed at 880, 1073, 1174, and 1403 cm^{-1}[29-32]. The signal of the BTO-NPs is almost negligible compared to the PVDF-related peaks. Analysis of the peaks shows (except for a small peak at 763 cm^{-1} corresponding to the α phase) that the PVDF composites consist predominantly of β and γ phases, which possess piezoelectric properties[29-32]. The ratio of β-to-γ phases (β/γ) and the fraction of electroactive phases (F_{EA}) in the PVDF can be calculated using the following equations[30,31],

$$\beta/\gamma = \frac{A_{1275}}{A_{1234}} \tag{1}$$

$$F_{EA} = \frac{A_{840}}{1.26\,A_{763} + A_{840}} \tag{2}$$

where A_{1275}, A_{1234}, A_{840}, and A_{763} are the intensities of the peaks at 1275, 1234, 840, and 763 cm^{-1}. The β-to-γ ratio and F_{EA} are estimated to be 1.1167 and 0.8396, respectively, from Figure 2A, leading to the relative amounts of β, γ, and α phases being ~0.44, ~0.40, and ~0.16, respectively. Figure 2B shows the X-ray diffraction (XRD) 2θ scan of the same film. The peaks related to the various planes of BTO confirm the presence of BTO-NPs. The peak near 20° is related to PVDF as the sum of the diffractions from β phase (200) and γ phase (101)[29-32]. The peaks at 24° and 33.76° corresponding to the (111) and (200) planes of $BaCO_3$; this byproduct arises from the reaction with CO_2 during the synthesis of the BTO-NPs. Figure 2C shows the XRD 2θ-ω scan of sputtered AlN thin films on Cu foil. The (002) and (004) peaks at 36.02° and

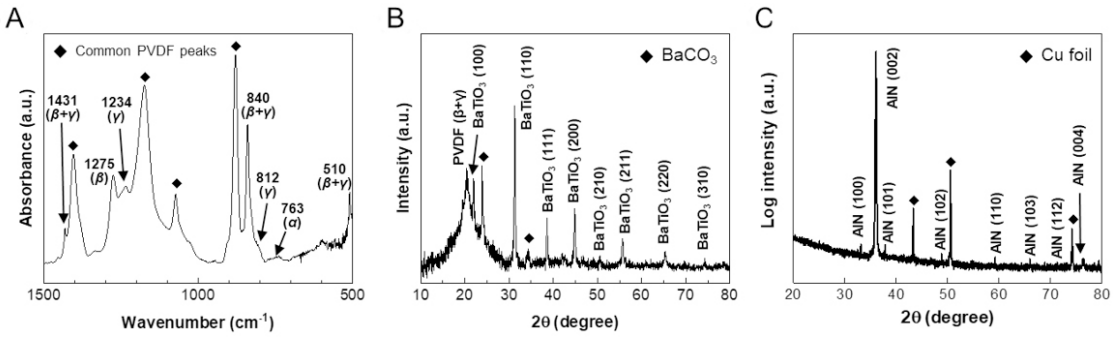

Figure 2. Characterization results of the films. (A) FTIR and (B) XRD of PVDF+BTO film. (C) XRD of AlN on Cu foil. FTIR: Fourier-transform infrared spectroscopy; PVDF: polyvinylidene fluoride; BTO: $BaTiO_3$; AlN: aluminum nitride.

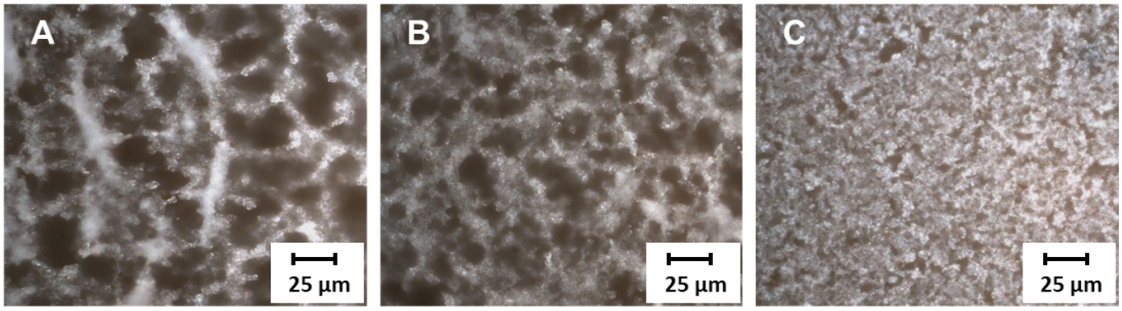

Figure 3. Optical microscope images of PVDF films with (A) 5 wt.%; (B) 10 wt.%; and (C) 30 wt.% BTO-NPs. PVDF: Polyvinylidene fluoride; BTO-NP: $BaTiO_3$ nanoparticle.

76.2°, respectively, are dominant, suggesting that the AlN films consist mostly of uniaxial-textured wurtzite crystal grains with the *c*-axis aligned in the out-of-plane direction. The films also show various small peaks related to (100), (101), (102), (110), (103), and (112), suggesting that the AlN is polycrystalline containing grain boundaries, which can give rise to leakage currents. The other peaks at 43.26°, 50.3°, and 74.12° arise from the foil substrate and correspond to the (111), (200), and (220) planes of Cu, respectively.

Figure 3 shows optical microscope images of the PVDF films with selected contents of BTO-NPs: 5 wt.%, 10 wt.%, and 30 wt.%. The films with 5 wt.% and 10 wt.% [Figure 3A and B] show numerous macro-pores (larger than 20 μm), which hamper robust film fabrication. The PVDF films with 5 wt.% and 10 wt.% of BTO-NPs are easily exfoliated during the drying step on both Cu foil and sputtered-AlN/Cu mainly due to shrinkage. In contrast, the films with 30 wt.% BTO-NPs shows significantly reduced pore sizes [Figure 3C], which indicates the capacity for uniform coverage of the AlN thin films. As a result, the PVDF film is mechanically stable, resisting exfoliation from the substrate. A large number of BTO-NPs are dispersed in the PVDF/DMSO solution during mixing, which increases the interfacial area and synergistic interactions with the PVDF backbone[33]. Given these considerations, we focused on PVDF with 30 wt.% BTO-NPs for device fabrication.

Sensing mechanism and fundamental piezoelectric characteristics

Figure 4 illustrates the piezoelectric voltage generation from bending by external force or deflection. The sensor is attached to skin surfaces, which are mostly curved (e.g., chin, neck, finger, and wrist). The sensor can be further bent up or down on the surface of the human body, then released to the initial curved state by the movements of muscles or joints, leading to a change of polarization in the piezoelectric film. Cu foil

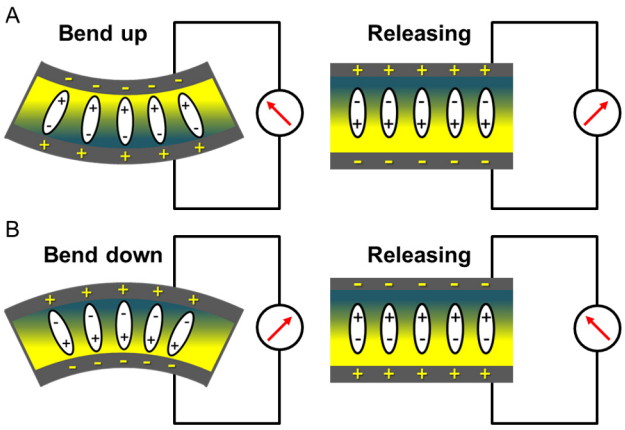

Figure 4. Sensing mechanism of piezoelectric sensor with (A) bend-up and (B) bend-down conditions followed by releasing to the initial state before bending.

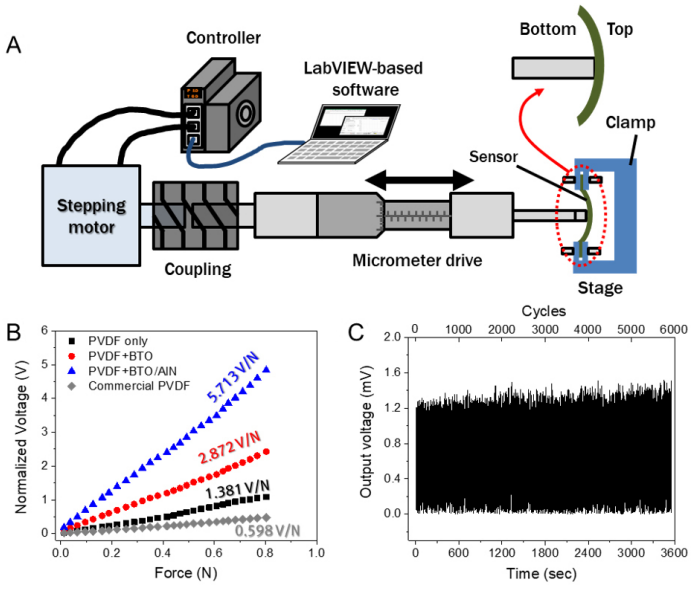

Figure 5. Characterization of electromechanical conversion of different piezoelectric films. (A) Schematic illustration of a custom-made piezoelectric test station; (B) electromechanical conversion in terms of applied force *vs.* output voltage of films normalized with 10-μm thickness; and (C) changes in output voltage over 5000 cycles using a repeated force of 0.2 N.

was selected as a substrate with greater thickness than the AlN film and similar elastic modulus to AlN, while maintaining sufficient mechanical flexibility, to have a neutral plane located in the Cu foil during the bending. Therefore, a single type of piezoelectric polarization change (positive or negative) is generated depending on the nature of the bending process. A bend-up condition [Figure 4A] generates negative and positive charges at the top and bottom electrodes, respectively. A bend-down condition [Figure 4B] induces opposite charges, that is, positive (top) and negative (bottom) charges. When the sensor is released from the bend-up or the bend-down conditions, reverse potential is generated across the top and bottom electrodes.

Figure 5A shows a custom-made piezoelectric test station consisting of a stepping motor, controller, micrometer drive, sample stage, and software to compare the electromechanical conversion performances of various piezoelectric films. The sensor on the sample stage is installed with a bottom electrode facing toward

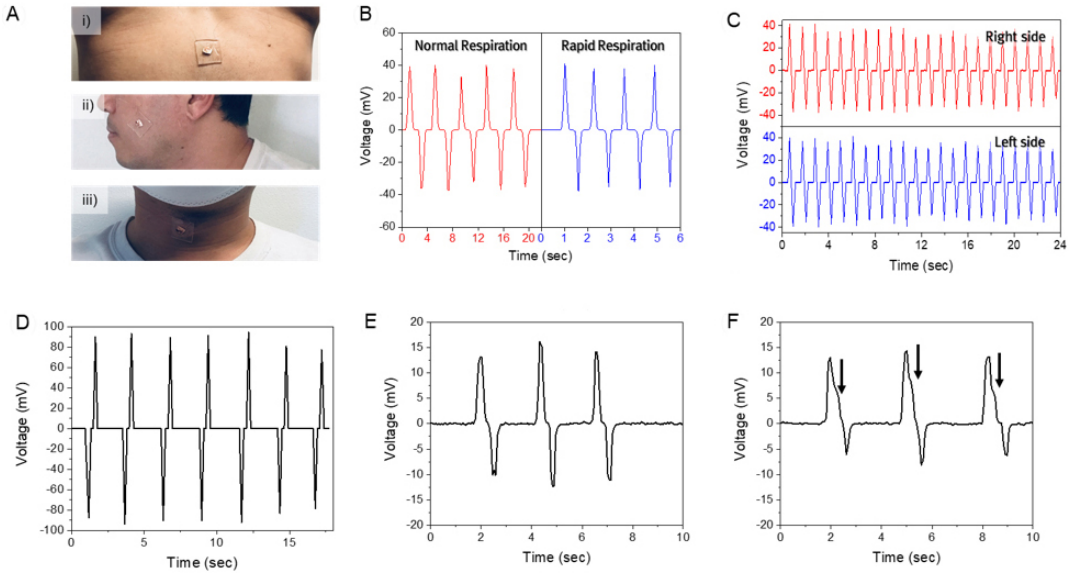

Figure 6. Piezoelectric pressure sensor for muscle motion monitoring. (A) Photographs of the sensor positions such as (i) diaphragm; (ii) jaw; and (iii) neck. The output voltages from (B) normal and rapid respiration, (C) chewing; and (D) swallowing. The output voltages from vocal stimulus (E) "Hi" and (F) "Houston". The arrows indicate the second syllable.

the micrometer drive to simulate the sensor attached to the skin. When the micrometer drive moves forward, the sensor is further bent down. Thus, the sensor generates positive potentials, as shown in Figure 5B, which are matched with the mechanism described in Figure 4. The output voltages of various films are compared in Figure 5B. The output voltages are normalized with a fixed thickness (e.g., 10 μm). The PBA film generates a higher voltage than the PVDF+BTO-NP and PVDF-only films. At 0.2 N, the PVDF, BTO-NP+PVDF, and PBA films exhibit 0.247, 0.639, and 1.28 V, respectively. In addition, a linear relationship in output *vs.* force shows good linearity in the sensitivity. The sensitivity of PBA is 5.713 V/N, which is nearly ten times higher than that of commercial PVDF films. The durability of the PBA sensor using a repeated force of 0.2 N over 5000 cycles is confirmed by no sign of degradation in the output signals in Figure 5C.

Sensing human activities and motions

The results of a series of experiments are shown to demonstrate the performance of the sensor for practical applications of human-motion monitoring. The response time is 4 to 6 ms in the overall condition, which is influenced by noise and limited by the transient data collection frequency. The PBA-PPS was attached to the chest, cheek, and throat to detect signals from the respiration, masticatory, and esophageal muscular movements, respectively, as shown in Figure 6A with the locations of the sensor. Figure 6B shows the output voltage from breathing. When the subject inhales, the sensor is further bent down by the deformation of the chest for expansion, then released during exhalation by contraction. The peak voltages are ~40 mV for both normal and rapid respiration. Then, chewing activity from cheek positions while the subject chewed gum every 0.5 seconds during the test was monitored. The sensor signals from the masticatory movement are shown in Figure 6C. Similar to the output from the breathing studies, a positive potential was first generated, followed by negative potential from the expansion and contraction of the cheek. The average peak voltages were ~35.7 and ~35.3 mV for the right and left sides, respectively, which can be utilized for a simple diagnosis of facial asymmetry. The human subject in this example showed only ~0.4 mV difference in average output value from the right and left cheeks. Both the output voltages from the right and left cheeks showed peak and flat regions, which might arise from hyolaryngeal muscle

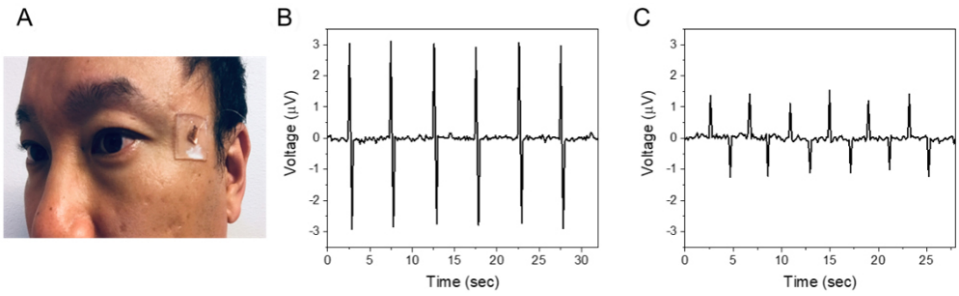

Figure 7. Sensing of eye blinking and eyeball movement. (A) Image of the sensor attached to the temple area. Voltage output characteristics of (B) eye blinking and (C) lateral eyeball movement.

movement[34,35]. As shown in Figure 6D, the sensor was also mounted on the throat to monitor the changes during water swallowing. The generated peak voltage value was ~94.3 mV with an average of ~88.1 mV, which is two times higher than those from breathing and chewing. In this case, the negative output was first generated because the sensor was bent-up and then released on the throat due to swallowing. The sensitivity of vocal stimulus was also investigated by fixing the sensor on a subject's throat [Figure 6Aiii]. Two output signals corresponding to "Hi" and "Houston" are shown in Figure 6E and F. In Figure 6E, "Hi" has only one syllable; thus, it showed a single positive and negative peak. In contrast, "Houston" with two syllables generated a satellite peak along the main peak, marked as arrows in Figure 6F. Here, a clear difference in the output voltage curves was observed due to different pressures and movements of the vocal cords during speech.

We further investigated the sensor for subtle deflections by muscle movements such as eye blinking and eyeball movement[10,16,17,36]. Since abnormal eye movements might be associated with several brain-related abnormalities, the detection of muscle movements near the eyes is important for the early diagnosis of the abnormalities. According to our previous study[36], the temple area is the ideal location to attach the sensor, as shown in Figure 7A. The output voltages with blinking and lateral eyeball motion as a function of measuring time are shown in Figure 7B and C, respectively. The sensor on the temple was bent down during eye blinking and transverse eyeball movement[36], giving rise to positive and negative potentials. The sensor was able to detect tiny deflections of the skin by eye movements, which is also useful in biomedical applications such as pulse monitoring. However, the generated voltage values are small (1 to 3 μV). The signal-to-noise ratio (SNR) is ~30 dB for the eye blinking, which might be too low for stable wireless communication.

Humans have several joints in their bodies that are crucial for daily activity. Bending characteristics of joints, including wrist, finger, and elbow, were examined and are shown in Figure 8. The PBA sensor was attached to the wrist for the detection of two types of distinguished motions (wrist-up and wrist-down), as shown in Figure 8A and B, respectively. When the wrist moved upward, the PBA sensor was bent up, and the corresponding peak voltage was negative 55 mV. Conversely, for downward bending, the sensor generated a peak output of positive 24.1 mV. The difference in peak output values from wrist-up and wrist-down motions is related to the difference in bending degree[37]. For other applications of large joint monitoring, elbow bending and releasing motions were investigated with the attachment of the sensor on the outer elbow. When the elbow was bent and released, electrical signals with positive and negative values were generated. Figure 8C demonstrates higher voltage values (≈ 252 mV) from the elbow joint due to the enhancement of stress and strain. Also, the PBA sensor was attached to the finger knuckle for the detection of small joint changes with various bending degrees. The generated voltage was proportional to the degree of bending, shown in Figure 8D, with the maximum voltages of 39.1, 55.2, and 74.7 mV for 30°, 60°, and 90°,

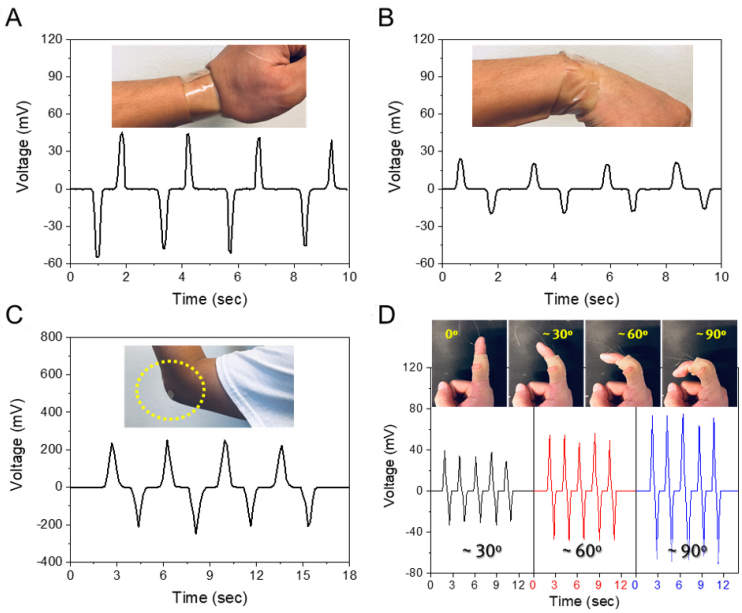

Figure 8. The piezoelectric PBA sensor characteristics from several joint motions. Voltage outputs of different types of wrist movements: (A) upward and (B) downward bending. Monitoring the bending amplitude of joints with the help of a Band-Aid; (C) elbow; and (D) finger with various bending angles. Inset photos represent the position where the PBA sensor was attached. PBA: PVDF+BTO-NP/AlN.

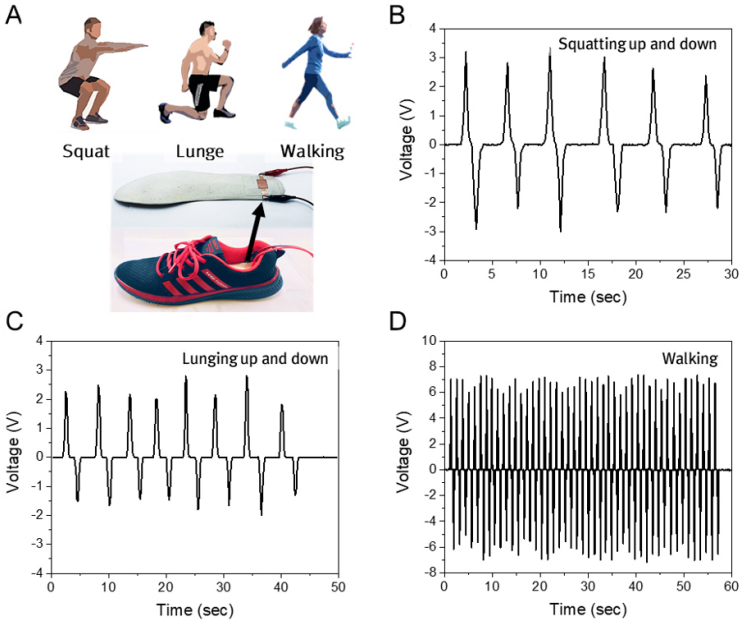

Figure 9. The piezoelectric performance of pressure sensing. (A) Illustration of practices and photographs of PBA sensor located in the insole of a shoe. The voltage output of pressure arising from (B) squatting; (C) lunging; and (D) walking. PBA: PVDF+BTO-NP/AlN.

respectively. These results demonstrate that different bending degrees can be distinguished by the output value. Also, each joint part generated different levels of voltages according to the stress and strain level. Furthermore, the movements of these limb parts can be useful for developing intelligent robot sensing and rehabilitation monitoring[38,39].

The piezoelectric sensors can be further utilized for energy harvesters. Among human motions, weight-based activities such as squatting, lunging, and walking [as shown in Figure 9A top] can apply high pressure and force, which can generate high potential values. The PBA sensor was installed into the insole of a shoe [Figure 9A bottom] worn by a subject having 70 kg of weight. As shown in Figure 9B-D, the peak voltages were 3.33, 2.81, and 7.37 V for squatting, lunging, and walking, respectively, which are relatively high output values. In this study, while we apply a single sensor to demonstrate the feasibility, the output values can be further enhanced for real applications of energy harvesters when the PBA sensor is comprised of arrays of multiple sensors.

CONCLUSIONS

In this study, we introduced a PBA sensor composed of BTO-NPs embedded in PVDF-coated AlN thin films. AlN was deposited on flexible Cu foil by RF-magnetron sputtering, and BTO-NP-dispersed PVDF was prepared by solution casting and spin-coating methods. The prepared sensor was analyzed by Raman, FTIR, and XRD. The physicochemical analyses showed piezoelectric phases of PVDF after heat-treatment and drying steps, which improved the piezoelectric properties of the PBA sensors. Basic piezoelectric performance was tested using a custom-made test station, and detailed parameters were controlled by computer software. With increasing applied force, the output voltage of the PBA sensor increased with a sensitivity of 5.713 V/N, which is the highest value among the compared materials. The durability of the PBA sensor was also confirmed up to 6000 cycles. We tested our sensor using various types of practical piezoelectric environments such as muscle movements, including vocal cord, eye-related motions, joint bending, and high pressure-bearing areas. The results indicate that several physiological signs generated distinguished outputs according to the range of bending forces from tiny deflections to high forces. The PBA sensors showed enhanced piezoelectric performance and sensitivity by applying PVDF+BTO-NP on AlN, which enables the PBA sensor competitive for bio-medical applications with wearable properties and energy-harvesting capabilities.

DECLARATIONS

Authors' contributions

Conceptualization: Kim NI, Lee TR, Ryou JH,
Methodology: Kim NI, Lee JM, Mina M, Chen J, Pouladi S, Yarali M, Lee TR, Ryou JH
Software: Kim NI, Lee JM, Chen J
Formal analysis: Kim NI, Lee JM
Writing - original draft preparation: Kim NI, Lee JM, Kim JY, Kwon MK
Writing - review and editing: Lee TR, Ryou JH

Availability of data and materials

The data presented in this study are available on request from the corresponding authors.

Financial support and sponsorship

This research was funded by Advanced Manufacturing Institute (AMI) at the University of Houston and the Texas Center for Superconductivity at the University of Houston (TcSUH). Additional support was provided by the Air Force Office of Scientific Research (AFOSR FA9550-20-1-0349; 20RT0302) and the Robert A. Welch Foundation (Grant No. E-1320).

Conflicts of interest

All authors declared that there are no conflicts of interest.

Ethical approval and consent to participate

Not applicable.

Consent for publication

Not applicable.

REFERENCES

1. Schwartz G, Tee BC, Mei J, et al. Flexible polymer transistors with high pressure sensitivity for application in electronic skin and health monitoring. *Nat Commun* 2013;4:1859. DOI PubMed
2. Arakawa M, Kudo K, Kobayashi K, Kanai H. Blood pressure measurement using piezoelectric effect by an ultrasonic probe. *Sens Actuators A Phys* 2019;286:146-51. DOI
3. Dagdeviren C, Su Y, Joe P, et al. Conformable amplified lead zirconate titanate sensors with enhanced piezoelectric response for cutaneous pressure monitoring. *Nat Commun* 2014;5:4496. DOI PubMed
4. Park DY, Joe DJ, Kim DH, et al. Self-powered real-time arterial pulse monitoring using ultrathin epidermal piezoelectric sensors. *Adv Mater* 2017;29:1702308. DOI PubMed
5. Wang TW, Lin SF. Wearable piezoelectric-based system for continuous beat-to-beat blood pressure measurement. *Sensors (Basel)* 2020;20:851. DOI PubMed PMC
6. Chiu Y, Lin W, Wang H, Huang S, Wu M. Development of a piezoelectric polyvinylidene fluoride (PVDF) polymer-based sensor patch for simultaneous heartbeat and respiration monitoring. *Sens Actuators A Phys* 2013;189:328-34. DOI
7. Lei KF, Hsieh YZ, Chiu YY, Wu MH. The structure design of piezoelectric poly(vinylidene fluoride) (PVDF) polymer-based sensor patch for the respiration monitoring under dynamic walking conditions. *Sensors (Basel)* 2015;15:18801-12. DOI PubMed PMC
8. Su Y, Chen C, Pan H, et al. Muscle fibers inspired high-performance piezoelectric textiles for wearable physiological monitoring. *Adv Funct Mater* 2021;31:2010962. DOI
9. Jin C, Hao N, Xu Z, et al. Flexible piezoelectric nanogenerators using metal-doped ZnO-PVDF Films. *Sens Actuators A Phys* 2020;305:111912. DOI PubMed PMC
10. Chen J, Liu H, Wang W, et al. High durable, biocompatible, and flexible piezoelectric pulse sensor using single-Crystalline III-N Thin Film. *Adv Funct Mater* 2019;29:1903162. DOI
11. Park JH, Jang DG, Park JW, Youm SK. Wearable sensing of in-ear pressure for heart rate monitoring with a piezoelectric sensor. *Sensors (Basel)* 2015;15:23402-17. DOI PubMed PMC
12. Guo W, Tan C, Shi K, et al. Wireless piezoelectric devices based on electrospun PVDF/$BaTiO_3$ NW nanocomposite fibers for human motion monitoring. *Nanoscale* 2018;10:17751-60. DOI PubMed
13. Khadtare S, Ko EJ, Kim YH, Lee HS, Moon DK. A flexible piezoelectric nanogenerator using conducting polymer and silver nanowire hybrid electrodes for its application in real-time muscular monitoring system. *Sens Actuators A Phys* 2019;299:111575. DOI
14. Liu Z, Zheng Q, Shi Y, et al. Flexible and stretchable dual mode nanogenerator for rehabilitation monitoring and information interaction. *J Mater Chem B* 2020;8:3647-54. DOI
15. Zhu J, Zhou C, Zhang M. Recent progress in flexible tactile sensor systems: from design to application. *Soft Sci* 2021;1:3. DOI
16. Lee S, Bae S, Lin L, et al. Super-flexible nanogenerator for energy harvesting from gentle wind and as an active deformation sensor. *Adv Funct Mater* 2013;23:2445-9. DOI
17. Lee S, Hinchet R, Lee Y, et al. Ultrathin nanogenerators as self-powered/active skin sensors for tracking eye ball motion. *Adv Funct Mater* 2014;24:1163-8. DOI
18. Yang Y, Pan H, Xie G, et al. Flexible piezoelectric pressure sensor based on polydopamine-modified BaTiO3/PVDF composite film for human motion monitoring. *Sens Actuators A Phys* 2020;301:111789. DOI
19. Yu J, Zhang K, Deng Y. Recent progress in pressure and temperature tactile sensors: Principle, classification, integration and outlook. *Soft Sci* 2021;1:6. DOI
20. Kim N, Chang Y, Chen J, et al. Piezoelectric pressure sensor based on flexible gallium nitride thin film for harsh-environment and high-temperature applications. *Sens Actuators A Phys* 2020;305:111940. DOI
21. Dagdeviren C, Hwang SW, Su Y, et al. Transient, biocompatible electronics and energy harvesters based on ZnO. *Small* 2013;9:3398-404. DOI PubMed
22. Chen J, Oh SK, Nabulsi N, Johnson H, Wang W, Ryou J. Biocompatible and sustainable power supply for self-powered wearable and implantable electronics using III-nitride thin-film-based flexible piezoelectric generator. *Nano Energy* 2019;57:670-9. DOI
23. Chen J, Oh SK, Zou H, et al. High-output lead-free flexible piezoelectric generator using single-crystalline gan thin film. *ACS Appl Mater Interfaces* 2018;10:12839-46. DOI PubMed
24. Cheng H. Preparation of [002] oriented AlN thin films by mid frequency reactive sputtering technique. *Thin Solid Films* 2003;425:85-9. DOI

25. Zembutsu S, Kobayashi M. The growth of c-axis-oriented GaN films by D.C.-biased reactive sputtering. *Thin Solid Films* 1985;129:289-97. DOI
26. Pawar S, Kumar A, Kaur D. Strain-induced dielectric enhancement in AlN-based multiferroic layered structure. *Shap Mem Superelasticity* 2020;6:24-8. DOI
27. Schneider M, Bittner A, Schmid U. Impact of film thickness on the temperature-activated leakage current behavior of sputtered aluminum nitride thin films. *Sens Actuators A Phys* 2015;224:177-84. DOI
28. Li J, Inukai K, Takahashi Y, Shin W. Synthesis and size control of monodispersed $BaTiO_3$ - PVP nanoparticles. *J Asian Ceram Soc* 2018;4:394-402. DOI
29. Gregorio R, Ueno EM. Effect of crystalline phase, orientation and temperature on the dielectric properties of poly (vinylidene fluoride) (PVDF). *J Mater Sci* 1999;34:4489-500. DOI
30. Cai X, Lei T, Sun D, Lin L. A critical analysis of the α, β and γ phases in poly(vinylidene fluoride) using FTIR. *RSC Adv* 2017;7:15382-9. DOI
31. Gregorio R. Determination of the α, β, and γ crystalline phases of poly(vinylidene fluoride) films prepared at different conditions. *J Appl Polym Sci* 2006;100:3272-9. DOI
32. Gregorio R, Cestari M. Effect of crystallization temperature on the crystalline phase content and morphology of poly(vinylidene fluoride). *J Polym Sci B Polym Phys* 1994;32:859-70. DOI
33. Yilmaz G, Lu X, Ho GW. Cross-linker mediated formation of sulfur-functionalized V_2O_5/graphene aerogels and their enhanced pseudocapacitive performance. *Nanoscale* 2017;9:802-11. DOI PubMed
34. Kim SH, Oh BM, Han TR, Jeong HJ, Sim YJ. Different movement of hyolaryngeal structures by various application of electrical stimulation in normal individuals. *Ann Rehabil Med* 2015;39:535-44. DOI PubMed PMC
35. Watts CR. Measurement of hyolaryngeal muscle activation using surface electromyography for comparison of two rehabilitative dysphagia exercises. *Arch Phys Med Rehabil* 2013;94:2542-8. DOI PubMed
36. Kim N, Chen J, Wang W, et al. Highly-sensitive skin-attachable eye-movement sensor using flexible nonhazardous piezoelectric thin film. *Adv Funct Mater* 2021;31:2008242. DOI
37. Yang YF, Tao LQ, Pang Y, et al. An ultrasensitive strain sensor with a wide strain range based on graphene armour scales. *Nanoscale* 2018;10:11524-30. DOI PubMed
38. Zhou H, Hu H. Human motion tracking for rehabilitation - A survey. *Biomed Signal Process Control* 2008;3:1-18. DOI
39. Maciejasz P, Eschweiler J, Gerlach-Hahn K, Jansen-Troy A, Leonhardt S. A survey on robotic devices for upper limb rehabilitation. *J Neuroeng Rehabil* 2014;11:3. DOI PubMed PMC